

Charm-strange meson production in ultra-relativistic heavy-ion collisions at the CERN-LHC energies

Shuang Li^{1,2,*} and Chaowen Wang^{1,†}

¹College of Science, China Three Gorges University, Yichang 443002, China

²Key Laboratory of Quark and Lepton Physics (MOE),
Central China Normal University, Wuhan 430079, China

(Dated: July 12, 2021)

The nuclear modification factor R_{AA} and the elliptic flow coefficient v_2 of charm-strange meson D_s^+ is systematically studied in Pb-Pb collisions at $\sqrt{s_{NN}} = 5.02$ TeV and 2.76 TeV. During the modeling, the coupling strength between the injected charm quark and the incident medium constituents, is extracted from the lattice QCD calculations: $2\pi TD_s = 7$ (**Model-A**) and $2\pi TD_s = 1.3 + (T/T_c)^2$ (**Model-B**). We find that, comparing $R_{AA}(D_s^+)$ with $R_{AA}(non-strange)$, the heavy-light coalescence effect is more pronounced for the former one, resulting in an enhancement behavior in the range $2 \lesssim p_T \lesssim 5$ GeV. The predictions for $R_{AA}(D_s^+)$ and $R_{AA}(non-strange)$ favor Model-A to have a better description of the measured p_T dependence in both energies, while their v_2 prefer Model-B at moderate p_T ($2 \lesssim p_T \lesssim 4$ GeV). Therefore, it is necessary to consider the temperature- and/or momentum-dependence of $2\pi TD_s$ to describe simultaneously $R_{AA}(D_s^+)$ and $v_2(D_s^+)$ in different centrality classes in Pb-Pb collisions.

I. INTRODUCTION

Ultra-relativistic heavy-ion collisions provide the unique opportunity to produce and study the properties of the strongly-interacting matter within the extreme high temperature and energy density environment, where a phase transition is expected from the ordinary hadron state to its deconfined constituents, namely Quark-Gluon Plasma (QGP) [1, 2]. Heavy quarks (HQ) such as charm and bottom are of particular interest amongst the various probes of the QGP [3–5]. Due to the large mass, they are mainly produced at the early stage of the collisions via the hard scattering process, and subsequently interact with the QGP constituents without affecting their mass, resulting in the negligible re-generation propagating through the medium. Meanwhile, the HQ flavour is conserved during the interaction with QGP constituents, therefore, the initial produced HQ will experience the full evolution of the hot and dense medium.

While traversing the QGP medium, a heavy quark will interact with the medium constituents and thus, lose part of its initial energy via both elastic ($2 \rightarrow 2$, collisional processes [6]) and inelastic scatterings ($2 \rightarrow 2 + X$, including gluon radiation [7]), naming the collisional and radiative energy loss, respectively. The energy loss effect together with the HQ hadronization mechanisms can be investigated by measuring the nuclear modification factor

$$R_{AA}(p_T, y) = \frac{d^2\sigma_{AA}/dp_T dy}{d^2\sigma_{pp}/dp_T dy}, \quad (1)$$

of the final heavy-flavor productions such as the open charmed mesons (i.e. D mesons including D^0 , D^+ , D^{*+}

and D_s^+ [8]), where, $d^2\sigma_{AA}/dp_T dy$ is the p_T and y double-differential production cross section in nucleus-nucleus collisions, scaled by the number of binary nucleon-nucleon collisions; $d^2\sigma_{pp}/dp_T dy$ is the double-differential result in nucleon-nucleon collisions. The deviation of R_{AA} from unity is sensitive to the nuclear effects, e.g. the initial (anti-)shadowing and the subsequent in-medium energy loss. In addition, the elliptic flow coefficient

$$v_2 = \left\langle \frac{p_x^2 - p_y^2}{p_x^2 + p_y^2} \right\rangle, \quad (2)$$

allows to describe the anisotropy of the transverse momentum, hence, v_2 is sensitive to the EoS and initial conditions in the low p_T region, and it is also able to reflect path-length-dependence of the energy loss at high p_T .

Many models were developed [9–14] to study the comprehensive sets of the available measurements of non-strange charmed meson, e.g. D^0 , D^+ and D^{*+} . It was realized [15–18] that the simultaneous description of their R_{AA} and v_2 requiring further understanding of the temperature-dependence of the coupling strength ($2\pi TD_s$) between the injected (heavy) quark and the incident medium constituent. The charm-strange meson $D_s^+(c\bar{s})$ production is more interesting with respect to non-strange charmed mesons, since its valence quark content consists of charm and (anti-)strange quark, which will couple the well-know strangeness enhancement [19]. D_s^+ spectra will be therefore affected by both the charm conservation and the strangeness enhancement effects in heavy-ion collisions. However, few models [20] were dedicated to investigate the D_s^+ meson spectra, as well as its R_{AA} and v_2 until now.

Based on the previous work, we try to address this question by taking into account the various temperature-dependence of $2\pi TD_s$ which are phenomenologically extracted from the lattice QCD calculation, and then investigate their effects on the observables (R_{AA} and v_2),

* lish@ctgu.edu.cn

† wangchaowen@ctgu.edu.cn

in particular for the charm-strange meson D_s^+ at the LHC energies. Meanwhile, as pointed in Ref. [21], we will explore the propagation of theoretical uncertainties in energy-loss predictions, for instance the pp baseline calculation and the (anti)-shadowing parameterization, in this analysis.

This paper proceeds as follows: Section II is dedicated to the introduction of the general steps of our hybrid model, including the initial condition, hydrodynamics expansion of the fireball, heavy quark Brownian motion and the subsequent hadronization processes. Section III presents the results such as the production cross section, R_{AA} and v_2 of D_s^+ meson in pp and Pb-Pb collisions. The comparison with available measurements are performed as well. Section IV contains the summary and conclusion.

II. METHODOLOGY

We construct a theoretical framework [22] to study the charm quark evolution in ultra-relativistic heavy-ion collisions. The general steps are outlined as follows, as well as the estimation of the theoretical uncertainties.

A. Hybrid Model Construction

1. Initial conditions for the hydrodynamical evolution

The initial spatial distribution of heavy quark pairs is sampled according to the initial entropy density distributions. The relevant transverse profile is modeled by a Glauber-based approach [23], while the longitudinal profile is described by a data-inspired phenomenological function [22]. The initial momentum distribution of heavy quark pairs is obtained via the FONLL calculations [24–26]. Finally, the $c\bar{c}$ is generated in back-to-back before including nuclear shadowing effect [27].

The initial entropy density distributions will be taken as input of the subsequent hydrodynamical evolution, which can be described by utilizing a 3+1 dimensional relativistic viscous hydrodynamics model [28] with the start time scale $\tau_0 = 0.6$ fm/c and the shear viscosity $\eta/s = 1/(4\pi)$. The tuning parameters in these modules are determined by the model-to-data comparison [22].

2. Heavy quark diffusion

The Brownian motion of charm quark when propagating through the Quark-Gluon Plasma (QGP), is described by utilizing the Langevin Transport Equation, and it can be modified to incorporate both the collisional and radiative energy loss processes, which reads [11]

$$dp = (F^{\text{Drag}} + F^{\text{Diff}} + F^{\text{Gluon}})dt, \quad (3)$$

with the drag force

$$F^{\text{Drag}} = -\Gamma(p) \cdot p, \quad (4)$$

the thermal random force[¶]

$$\langle F_i^{\text{Diff}}(t) \cdot F_j^{\text{Diff}}(t + n\Delta t) \rangle \equiv \frac{\kappa(p)}{\Delta t} \delta_{ij} \delta_{0n} \quad (5)$$

and the recoil force

$$F^{\text{Gluon}} = -\frac{dp^{\text{Gluon}}}{dt}. \quad (6)$$

p^{Gluon} indicates the momentum of the radiated gluon, which can be quantified by the pQCD Higher-Twist calculation [29]. It is assumed [11] that the fluctuation-dissipation relation is still validated between the drag (Eq. 4) and the diffusion terms (Eq. 5) in Eq. 3:

$$\Gamma(p) = \frac{\kappa(p)}{2TE}, \quad (7)$$

where, $\Gamma(p)$ and $\kappa(p)$ denote the drag and the momentum diffusion coefficients, respectively, and they can be rewritten via the spatial diffusion coefficient $2\pi TD_s$ [30],

$$\Gamma = \frac{1}{(2\pi TD_s)} \cdot \frac{2\pi T^2}{E}, \quad (8)$$

$$\kappa = \frac{1}{(2\pi TD_s)} \cdot 4\pi T^3. \quad (9)$$

Note that the definition of $2\pi TD_s$ is extended from zero-momentum to larger momentum region. As discussed in Ref. [22], $2\pi TD_s$ can be obtained by performing a phenomenological fit analysis with the lattice QCD calculations. Two approaches are summarized as follows:

• Model-A

$$2\pi TD_s = 7 \quad (10)$$

In this approach the drag coefficient behaves $\Gamma \propto T^2$, which is similar with the AdS/CFT or pQCD calculation [9].

• Model-B

$$2\pi TD_s = 1.3 + \left(\frac{T}{T_c}\right)^2 \quad (11)$$

where, T_c denotes the critical temperature. In this approach the drag coefficient behaves a weak T -dependence, which is consistent with the results shown in Ref. [17, 31].

[¶]Assuming an isotropic momentum-dependence of the diffusion coefficient with the post-point scheme.

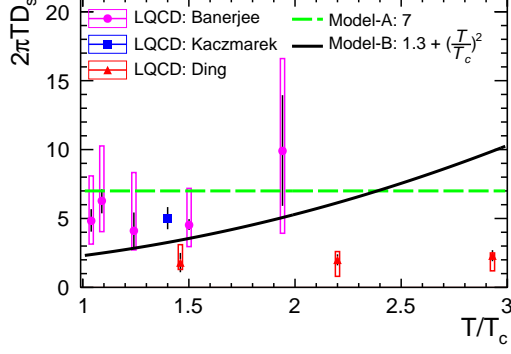


FIG. 1. (Color online) Charm quark spatial diffusion coefficient $2\pi T D_s$ calculated by the lattice QCD at zero momentum: pink circle [32], blue square [33] and red triangle [34]. The phenomenological approaches (dashed green and solid black curves) are displayed as well.

Figure 1 presents the T -dependence of $2\pi T D_s$ as calculated by the lattice QCD, i.e. Banerjee (pink circles [32]), Kaczmarek (blue square [33]) and Ding (red triangle [34]), as well as the results modeled via the two approaches, i.e. Model-A (dashed green curve; Eq. 10) and Model-B (solid black curve; Eq. 11). The corresponding results are summarized in Tab. I. It is found that most of the results obtained for the momentum diffusion coefficient κ/T^3 and HQ transport coefficient \hat{q}_Q/T^3 , are consistent with the other model predictions within the significant systematic uncertainties.

	Model-A	Model-B	Reference
$2\pi T D_s$	7	$1.3 + (\frac{T}{T_c})^2$	
$\frac{\kappa}{T^3} (\frac{T}{T_c} = 1.5)$	1.80	3.53	$1.8 \sim 3.4$ [35]
$\frac{\hat{q}_Q}{T^3} (\frac{T}{T_c} = 1.88)$	3.59	5.20	$3.4 \sim 5.8$ [36]
$\frac{\hat{q}_Q}{T^3} (\frac{T}{T_c} = 2.61)$	3.59	3.11	$2.3 \sim 5.1$ [36]

TABLE I. Summary of the different approaches for $2\pi T D_s$ as a function of temperature (see Fig. 1), as well as the relevant results obtained for κ/T^3 and \hat{q}_Q/T^3 . The other model predictions are shown for comparison.

For charm quark, the relevant thermalization time defined in zero momentum limit [30]

$$\tau_{charm} = \frac{m_{charm}}{2\pi T_c^2} \cdot \frac{2\pi T D_s}{(T/T_c)^2}, \quad (12)$$

is 3.03 and 2.29 fm/c for Model-A and Model-B, respectively, in Pb-Pb collisions at 2.76 and 5.02 TeV with $T = 2T_c = 330$ MeV and $m_{charm} = 1.5$ GeV.

Figure 2 shows the average in-medium energy loss of charm quarks as a function of the initial energy in central (0 – 10%) Pb-Pb collisions at $\sqrt{s_{NN}} = 5.02$ TeV, displaying separately the contributions of collisional (long

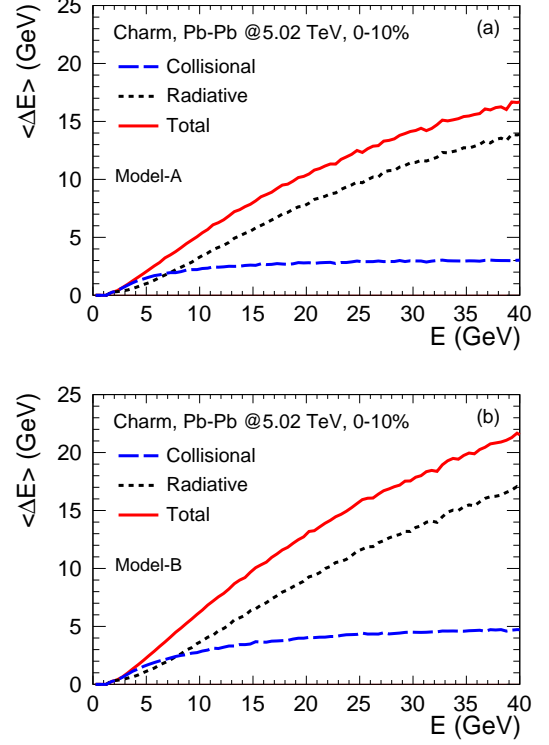


FIG. 2. (Color online) Energy loss of charm quarks obtained via (a) Model-A and (b) Model-B: collisional and radiative contributions are shown separately as long dashed blue and dashed black curves, respectively, in each panel. The combined results are shown as solid red curve.

dashed blue curve) and radiative (dashed black curve) mechanisms. The results based on Model-A (Eq. 10) are shown in the panel-a (upper). As pointed in Ref. [22], the collisional energy loss is significant at low energy, while radiative energy loss is the dominant mechanism at high energy. The crossing point between collisional and radiative contributions is around $E = 7 \sim 8$ GeV. Since the drag force is proportional to charm velocity $v = p/E$ (Eq. 4 and 8), in the low energy region ($E \lesssim 7 \sim 8$ GeV), where the relativistic effect is trivial ($E \propto v^2$), the collisional energy loss will be significant. However, in the very large energy region ($E \gtrsim 20$ GeV), where the ultra-relativistic effect should be taken into account ($E \propto 1/\sqrt{1-v^2}$ and $v \lesssim 1$), therefore, the collisional contribution will increase slowly at larger energy. In this case, the radiative energy loss will be the most dominant energy loss mechanisms. The results based on Model-B (Eq. 11) are displayed in the panel-b (bottom) of Fig. 2. A qualitatively similar trend can be found with Model-B, but with slightly stronger energy loss effects. This is caused by the fact that [22], (1) the underlying medium temperature drops rapidly from its initial value, and charm quark will stay longer at low temperature ($\sim 1 - 2T_c$); (2) the initial transverse momentum spectrum of charm quark is much more harder than that of medium constituent, thus, the multiple elastic scatterings among them are dominated by the drag term

rather than the diffusion term; (3) a larger drag coefficient near T_c with Model-B, stating a stronger interaction strength between the injected charm quark and the incident medium constituents, consequently, the charm quark allows to lose more its energy with Model-B approach.

3. Heavy quark hadronization

When the local temperature below the critical one $T_c = 165$ GeV, the charm quark will undergo the instantaneous hadronization via a “dual” approach, including fragmentation and heavy-light coalescence mechanisms. Concerning the universal fragmentation functions, various models are adopted in this work, e.g. Lund-PYTHIA 6.4 [37], Peterson [38], Collins-Spiller [39], Braaten [40] and FONLL-style [41], which are summarized in Tab. II. Apart from the Lund-PYTHIA, the fragmentation fractions for the various hadron species are $f(c \rightarrow D^0) = 0.566$, $f(c \rightarrow D^+) = 0.227$, $f(c \rightarrow D^{*+}) = 0.230$ and $f(c \rightarrow D_s^+) = 0.081$ [22], respectively, in the other approaches.

Name	Frag. Function	Parameter
Lund-PYTHIA	Eq. 12.11 in Ref. [37]	Default ones
Peterson	Eq. 4 in Ref. [38]	$\epsilon_c = 0.06$
Collins-Spiller	Eq. 20 in Ref. [39]	$\epsilon_c = 0.01$
Braaten	Eq. 9 and 12 in Ref. [40]	$r = \frac{m_{hadron} - m_c}{m_{hadron}}$
FONLL-style	Eq. 9 and 12 in Ref. [40]	$r = 0.1$ [41]

TABLE II. Summary of the different fragmentation functions, as well as the relevant parameters. Note that m_{hadron} and m_c in Braaten are the mass of the open charmed hadron and its mother charm quark, respectively.

According to the heavy-light coalescence model [42], the momentum distributions of heavy-flavor mesons ($Q\bar{q}$) are given as

$$\frac{dN_M}{d^3\vec{p}_M} = g_M \int d^3\vec{x}_Q d^3\vec{p}_Q d^3\vec{x}_{\bar{q}} d^3\vec{p}_{\bar{q}} f_Q(\vec{x}_Q, \vec{p}_Q) f_{\bar{q}}(\vec{x}_{\bar{q}}, \vec{p}_{\bar{q}}) \bar{W}_M^{(n)}(\vec{y}, \vec{k}) \delta^{(3)}(\vec{p}_M - \vec{p}_Q - \vec{p}_{\bar{q}}) \quad (13)$$

where, g_M is the degeneracy factor; $f_Q(\vec{x}_Q, \vec{p}_Q)$ and $f_{\bar{q}}(\vec{x}_{\bar{q}}, \vec{p}_{\bar{q}})$ are the phase-space distributions of heavy quark and light anti-quark (i.e. the coalescence candidate), respectively. The coalescence probability for $Q\bar{q}$ combination to form the heavy-flavor meson in the n^{th} excited state, is quantified by

$$\bar{W}_M^{(n)}(\vec{y}, \vec{k}) = \frac{v^n}{n!} e^{-v}, \quad v = \frac{1}{2} \left(\frac{\vec{y}^2}{\sigma_M^2} + \sigma_M^2 \vec{k}^2 \right), \quad (14)$$

where,

$$\vec{y} = \vec{x}_Q - \vec{x}_{\bar{q}} \quad (15)$$

$$\vec{k} = (m_{\bar{q}}\vec{p}_Q - m_Q\vec{p}_{\bar{q}})/(m_Q + m_{\bar{q}})$$

are the relative coordinate and the relative momentum, respectively, in the center-of-mass frame of $Q\bar{q}$ pair. The width parameter σ_M can be written as [22]

$$\sigma_M^2 = \begin{cases} \frac{2}{3} \frac{(e_Q + e_{\bar{q}})(m_Q + m_{\bar{q}})^2}{e_Q m_{\bar{q}}^2 + e_{\bar{q}} m_Q^2} \cdot \langle r_M^2 \rangle & (n=0) \\ \frac{2}{5} \frac{(e_Q + e_{\bar{q}})(m_Q + m_{\bar{q}})^2}{e_Q m_{\bar{q}}^2 + e_{\bar{q}} m_Q^2} \cdot \langle r_M^2 \rangle & (n=1) \end{cases} \quad (16)$$

where, $\langle r_M^2 \rangle \approx (0.9 \text{ fm})^2$ is the mean-square charge radius of D-meson; e_Q and $e_{\bar{q}}$ are the absolute values of the charge of heavy quark and light anti-quark, respectively; the light (anti-)quark mass takes $m_{u/\bar{u}} = m_{d/\bar{d}} = 300$ MeV and $m_{s/\bar{s}} = 475$ MeV.

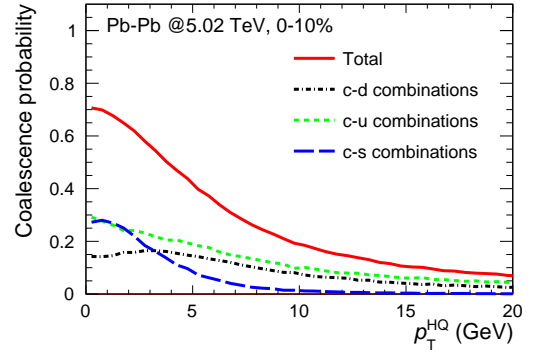


FIG. 3. (Color online) Comparison of the coalescence probability contributed by different combinations in central (0 – 10%) Pb–Pb collisions at $\sqrt{s_{NN}} = 5.02$ TeV: cd (dot-dashed black curve), cu (dashed green curve) and cs (long dashed blue curve). Both the ground states and the first excited states are considered. The combined results (solid red curve) are presented as well.

We consider the charm-strange meson species up to their first excited states ($n \leq 1$), which are listed in details in Ref. [22]. Figure 3 shows the coalescence probability obtained in central (0 – 10%) Pb–Pb collisions at $\sqrt{s_{NN}} = 5.02$ TeV, as a function of the charm quark transverse momentum (p_T). The results for the charm quark combined with down quark (cd), up quark (cu) and strange quark (cs) are presented as dot-dashed black, dashed green and long dashed blue curves, respectively. As shown in Eq. 14 and 16, the quark mass and its charge plays the role of the weighting factor in the heavy-light coalescence model, resulting in the difference among cd , cu and cs combinations. Moreover, this difference can also be induced at a certain amount by the thermal spectrum of u/d and s quark, which is steeper for the former one, indicating a larger probability to sample the light quark with small p_T . Finally, it is found that the charm quark prefers to coalesce with u and s quarks in the range $p_T \lesssim 3$ GeV. The total results (solid red curve) show a

decreasing behavior with increasing p_T , varying from 0.7 at $p_T \sim 0$ to 0.2 at $p_T \sim 10$ GeV, hence, the HQ with low/moderate and high p_T tends to hadronize via coalescence and fragmentation mechanisms, respectively.

Note that the coalescence candidates are sampled among various light (anti-)quarks, which are assumed to thermalize inside QGP. Therefore, we utilize the Fermi-Dirac approach, $f_q(\vec{p}) \propto (e^{\sqrt{\vec{p}^2 + m_q^2}/T_c} + 1)^{-1}$, to describe its density distribution, where m_q is the light (anti-)quark mass, and $T_c = 165$ MeV is the critical temperature. The flavor of the light (anti-)quark is determined according to the integrated parton density $\rho = \int_{-\infty}^{\infty} d^3\vec{p} f_q(\vec{p})$. For instance, $\rho_{u/d} = 0.18 \text{ fm}^{-3}$ for u/\bar{u} and d/\bar{d} quarks, and $\rho_s = 0.10 \text{ fm}^{-3}$ for s/\bar{s} quarks, resulting in the relative ratio $\rho_u : \rho_d : \rho_s \approx 1 : 1 : 0.5$, which is kept during the sampling procedure.

B. Theoretical Uncertainty

In this analysis, the total theoretical uncertainty consists of three components: FONLL predictions, nuclear shadowing and fragmentation models, which are added in quadrature for the final predictions.

The initial charm quark spectra are determined by the FONLL calculations [24], as well as the corresponding central values obtained by setting $\mu_R = \mu_F = \mu_0 \equiv \sqrt{p_T^2 + m_c^2}$, where, μ_R (μ_F) is the renormalization (factorization) scale; m_c denotes the heavy quark mass, and its central value is $m_c = 1.5$ GeV. The relevant uncertainties are estimated via a conservative approach [43]: $\mu_0/2 < \mu_R$, $\mu_F < 2\mu_0$, $\mu_R/2 < \mu_F < 2\mu_R$ and $1.3 < m_c < 1.7$ GeV.

The uncertainty on nuclear shadowing is estimated according to the various nPDFs sets in EPS09NLO parameterization, which are obtained by tuning the fit parameters to reproduce the available measurements [27]. In this work, we employ the nPDFs sets up to $k = 7$. See Eq. 2.12 and 2.13 in Ref. [27] for details.

Based on the different fragmentation scenarios (see Tab. II), the final observables such as the production cross section are close to each other. Therefore, we take the averaged results among them as the final one, and the maximum dispersion gives the theoretical uncertainty.

III. RESULTS

A. Production cross section in pp collisions

In Fig. 4 the p_T -differential production cross section of D_s^+ meson is predicted at mid-rapidity ($|y| < 0.5$) in pp collisions at $\sqrt{s} = 7$ TeV. The central value, upper band and the lower band are displayed as dashed, long dashed and solid curves, respectively. The uncertainty on FONLL calculations (50 ~ 100%) are dominated at $2 \lesssim p_T \lesssim 8$ GeV/c comparing with the one on frag-

mentation models ($\sim 30\%$ at maximum), while they are compatible ($\sim 30\%$) toward larger p_T . The experimental data (boxes) are shown for comparison. Within the experimental and theoretical uncertainties, the measured p_T dependence can be well described by the model predictions. Similar conclusion can be found in pp collisions at $\sqrt{s} = 5.02$ TeV.[¶]

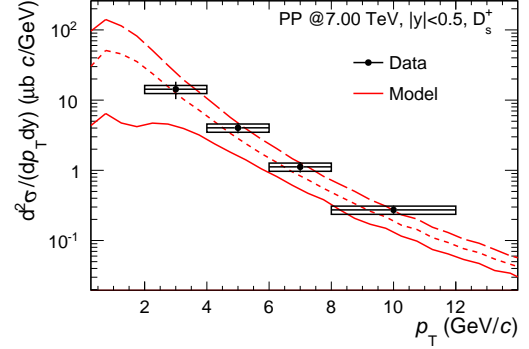


FIG. 4. (Color online) p_T -differential production cross section of D_s^+ meson with $|y| < 0.5$ in pp collisions at $\sqrt{s} = 7$ TeV. Experimental data taken from Ref. [45].

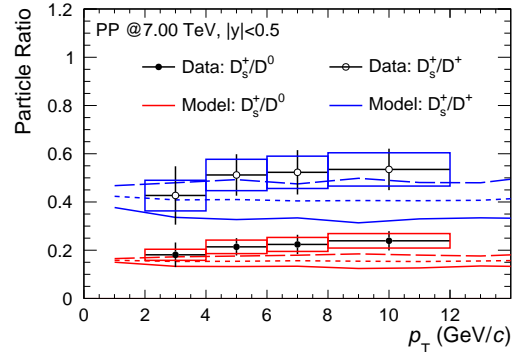


FIG. 5. (Color online) Ratios of D-meson production cross sections as a function of p_T . the measurements for D_s^+/D^0 (solid) and D_s^+/D^+ (empty) are shown as boxes, while the relevant model predictions displayed as the bands. Experimental data taken from Ref. [45].

Figure 5 presents the ratios of the charm-strange meson D_s^+ with respect to the non-strange charmed meson such as D^0 and D^+ , in pp collisions at $\sqrt{s} = 7$ TeV. See the legend for details. For both D_s^+/D^0 and D_s^+/D^+ , the theoretical uncertainty on FONLL calculation ($\sim 10\%$ at maximum) is dominated in the range $2 \lesssim p_T \lesssim 4$ GeV/c, while the one on fragmentation models ($\sim 20\%$ at maximum) at higher p_T . It is found that, within uncertainties, the measurements can be reproduced by the corresponding model predictions.

[¶] D_s^+ spectrum in pp collisions at $\sqrt{s} = 5.02$ TeV, is obtained via $d\sigma_{pp}/dp_T = R_{AA} \cdot d\sigma_{AA}/dp_T$, while the corresponding R_{AA} and $d\sigma_{AA}/dp_T$ are reported in Ref. [44].

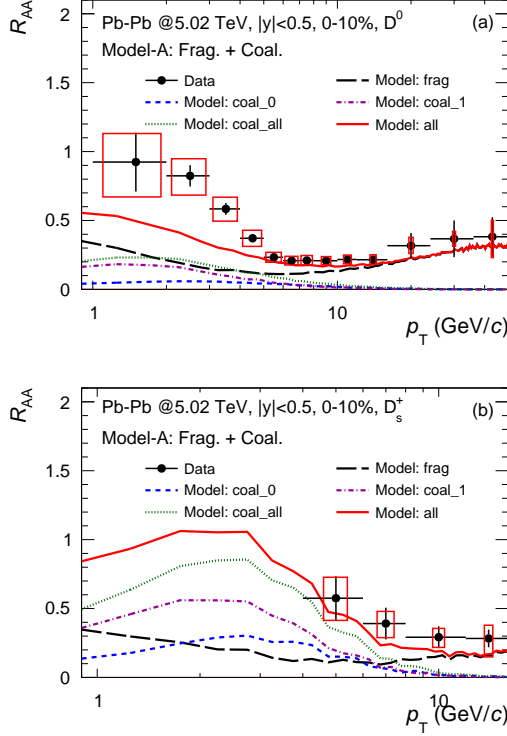


FIG. 6. (Color online) Comparison of the central predictions of R_{AA} contributed by different hadronization mechanisms, for (a) the non-strange charmed meson (average among D^0 , D^+ and D^{*+}) and (b) the charm-strange meson (D_s^+), at mid-rapidity ($|y| < 0.5$) in central (0 – 10%) Pb–Pb collisions at $\sqrt{s_{NN}} = 5.02$ TeV. See legend for details. Experimental data taken from Ref. [44].

B. Nuclear modification factor and Elliptic flow

The panel-a of Fig. 6 shows the average R_{AA} of non-strange charmed meson (D^0 , D^+ and D^{*+}) at mid-rapidity ($|y| < 0.5$), with Model-A approach (Eq. 10) in central (0 – 10%) Pb–Pb collisions at $\sqrt{s_{NN}} = 5.02$ TeV, which is contributed by the various hadronization mechanisms. It is found that the fragmentation component (long dashed black curve) is dominated at $p_T \gtrsim 7 - 8$ GeV/c, while the coalescence (dotted green curve) is significant at $1 \lesssim p_T \lesssim 5$ GeV/c, and furthermore, the first excited states contribution (dot-dashed purple curve) is more pronounced in this region. The central prediction (solid red curve) can describe the measurement in the range $p_T > 5$ GeV/c. R_{AA} of charm-strange meson (D_s^+) is presented in the panel-b of Fig. 6. Similar behavior is observed when comparing with the non-strange charmed mesons, however, the coalescence effect is more pronounced for D_s^+ meson. It is further checked that $R_{AA}(average)$ and $R_{AA}(D_s^+)$ calculated by considering alone the fragmentation mechanism, are close to each other. All the conclusions drawn above are the same as the ones found in semi-central (30 – 50%) Pb–Pb collisions at $\sqrt{s_{NN}} = 5.02$ TeV, as well as in Pb–Pb collisions at $\sqrt{s_{NN}} = 2.76$ TeV. Therefore, the future measure-

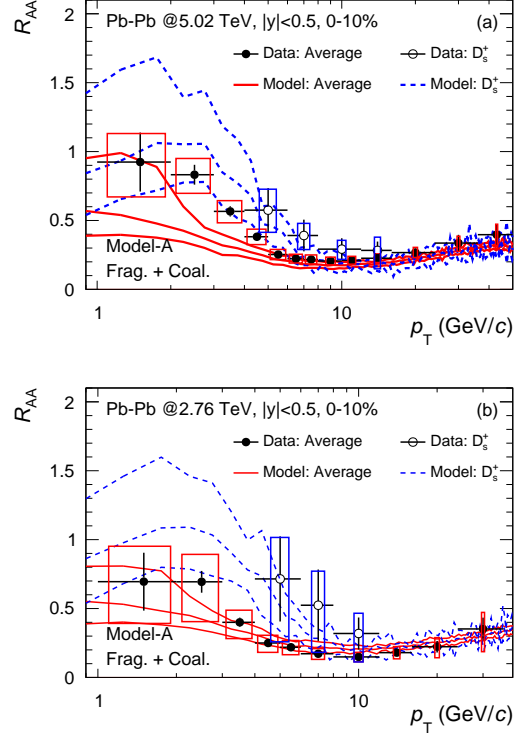


FIG. 7. (Color online) Comparison of R_{AA} for the average non-strange D mesons (solid red curves) and D_s^+ (dashed blue curves) predicted at mid-rapidity ($|y| < 0.5$) in central (0 – 10%) Pb–Pb collisions at (a) $\sqrt{s_{NN}} = 5.02$ TeV and (b) 2.76 TeV, respectively. Experimental data taken from Ref. [44, 46].

ments of $R_{AA}(D_s^+)$ with higher precision are more powerful to constrain the heavy-light coalescence effect at moderate p_T ($p_T = 2 \sim 5$ GeV/c).

$R_{AA}(average)$ (solid curves) and $R_{AA}(D_s^+)$ (dashed curves) obtained at mid-rapidity ($|y| < 0.5$), with Model-A approach in central (0 – 10%) Pb–Pb collisions at $\sqrt{s_{NN}} = 5.02$ TeV, are shown in the panel-a of Fig. 7. The results between average non-strange D-meson and D_s^+ are similar in the range $p_T \gtrsim 6$ GeV/c ($p_T \gg m_c$), while the latter one is systematically larger at $2 < p_T < 5$ GeV/c, resulting in an enhancement of D_s^+ production with respect to the average one. As mentioned in Fig. 6, the enhancement behavior is mainly induced by the coalescence mechanism during the charm quark hadronization. Note that, for $R_{AA}(average)$, the uncertainty on FONLL calculations ($\sim 80\%$ at maximum) are dominated at $1 < p_T < 3$ GeV/c, while the one on nuclear shadowing ($\lesssim 10\%$) and fragmentation functions ($\sim 10 - 15\%$) are significant at higher p_T . Similar behavior can be found for $R_{AA}(D_s^+)$ at low p_T , but the uncertainty on fragmentation functions ($\sim 20 - 40\%$) are dominated at $p_T > 3$ GeV/c. For comparison, the available measurements for the average non-strange D-meson (solid) and D_s^+ meson (empty) are displayed as well. Within the experimental and theoretical uncertainties, the model calculations can reproduce the data for both

the average and D_s^+ meson. Similar results are found in central (0 – 10%) Pb–Pb collisions at $\sqrt{s_{\text{NN}}} = 2.76$ TeV. See the panel-b of Fig. 7 for details.

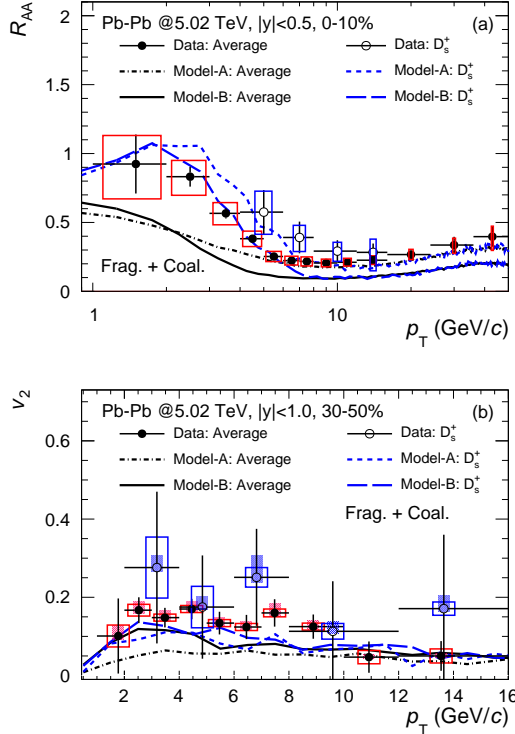


FIG. 8. Comparison between the average non-strange D mesons and D_s^+ observables obtained with Model-A and Model-B approaches in Pb–Pb collisions at $\sqrt{s_{\text{NN}}} = 5.02$ TeV: R_{AA} (upper) in 0 – 10% and v_2 in 30 – 50%. Experimental data taken from Ref. [44, 47].

To compare the predictions based on Model-A (Eq. 10) and Model-B approaches (Eq. 11), the panel-a of Fig. 8 presents $R_{\text{AA}}(\text{average})$ and $R_{\text{AA}}(D_s^+)$ calculated in central (0 – 10%) Pb–Pb collisions at $\sqrt{s_{\text{NN}}} = 5.02$ TeV. $R_{\text{AA}}(\text{average})$ is enhanced (suppressed) at low (high) p_T from Model-A (dot-dashed black curve) to Model-B (solid black curve), since the relevant $2\pi TD_s$ near T_c is smaller based on Model-B, the larger is its initial drag term, which is more powerful to pull $c\bar{c}$ pairs from high momentum to low momentum [22], as pointed in Sec. II A 2. The results between different models are close at $p_T \sim 2$ GeV/c. Similar behavior is observed for $R_{\text{AA}}(D_s^+)$. When comparing $R_{\text{AA}}(\text{average})$ with $R_{\text{AA}}(D_s^+)$, the results with Model-A approach are discussed already in the panel-a of Fig. 7, and same conclusion can be drawn with Model-B approach. The panel-b of Fig. 8 shows the elliptic flow coefficient v_2 predicted in semi-central (30 – 50%) Pb–Pb collisions at $\sqrt{s_{\text{NN}}} = 5.02$ TeV: both $v_2(\text{average})$ and $v_2(D_s^+)$ are

significantly enhanced at intermediate p_T ($2 \lesssim p_T \lesssim 4$ GeV/c) from Model-A (dot-dashed black curve) to Model-B (solid black curve). Performing the model-to-data comparison, it is realized that $R_{\text{AA}}(\text{average})$ and $R_{\text{AA}}(D_s^+)$ favor Model-A to have a better description of the measured p_T dependence, while their v_2 prefer Model-B at moderate p_T ($2 \lesssim p_T \lesssim 4$ GeV/c), indicating the necessity to consider the temperature- and/or momentum-dependence of $2\pi TD_s$ to describe simultaneously R_{AA} and v_2 for both the non-strange D-meson and D_s^+ meson.

IV. SUMMARY AND CONCLUSIONS

In this analysis, we aim to investigate the nuclear modification of D_s^+ meson spectra together with its elliptic flow in ultra-relativistic heavy-ion collisions. We utilize the theoretical framework built in our previous work to achieve this goal, and extend it to include further the theoretical uncertainty on initial charm quark spectra, nuclear shadowing and fragmentation model. The coupling strength for charm quark $2\pi TD_s$ is obtained by fitting the lattice QCD calculations: $2\pi TD_s = 7$ (**Model-A**, i.e. no temperature dependence) and $2\pi TD_s = 1.3 + (T/T_c)^2$ (**Model-B**, i.e. weak temperature dependence).

It is found that D_s^+ spectra measured at mid-rapidity ($|y| < 0.5$) can be well described by the relevant model predictions in pp collisions both at $\sqrt{s} = 7$ TeV and 5.02 TeV, as well as the derived particle ratios D_s^+/D^0 and D_s^+/D^+ . The nuclear modification factor $R_{\text{AA}}(D_s^+)$ is systematically larger than $R_{\text{AA}}(\text{non-strange})$ at intermediate p_T ($2 \lesssim p_T \lesssim 5$ GeV) in central (0 – 10%) and semi-central (30 – 50%) Pb–Pb collisions both at $\sqrt{s_{\text{NN}}} = 5.02$ TeV and 2.76 TeV, which is mainly induced by the heavy-light coalescence mechanism. Hence, the future measurements of $R_{\text{AA}}(D_s^+)$ with higher precision are more powerful to constrain the heavy-light coalescence effect at moderate p_T ($p_T = 2 \sim 5$ GeV/c). For the model-to-data comparisons, the predictions of $R_{\text{AA}}(D_s^+)$ and $R_{\text{AA}}(\text{non-strange})$ favor Model-A to reproduce well the measured p_T dependence in both colliding energies, while their v_2 prefer Model-B at moderate p_T ($2 \lesssim p_T \lesssim 4$ GeV), suggesting a temperature and/or momentum dependent $2\pi TD_s$ is needed to describe simultaneously the D-meson R_{AA} and v_2 data.

ACKNOWLEDGMENTS

The authors are grateful to Kejun Wu and Kyong Chol Han for the useful discussions. S. Li is supported by the CTGU No.1910103, B2018023, QLPL2018P01, NSFC No.11447023 and No.11875178. C. W. Wang acknowledges the support from the NSFHB No.2012FFA085.

-
- [1] M. Gyulassy and L. McLerran, *Nucl. Phys.* **A750**, 30 (2005).
 - [2] E. Shuryak, *Nucl. Phys.* **A750**, 64 (2005).
 - [3] F. Prino and R. Rapp, *J. Phys.* **G43**, 093002 (2016).
 - [4] J. Schukraft, *Nucl. Phys.* **A967**, 1 (2017).
 - [5] R. Rapp *et al*, [arXiv:1803.03824](#) (2018).
 - [6] S. Wicks, W. Horowitz, M. Djordjevic, and M. Gyulassy, *Nucl. Phys.* **A784**, 426 (2007).
 - [7] M. Gyulassy and X. N. Wang, *Nucl. Phys.* **B420**, 583 (1994).
 - [8] S. Li (for the ALICE Collaboration), *Nucl. Phys.* **A931**, 546 (2014).
 - [9] Y. Akamatsu, T. Hastuda, and T. Hirano, *Phys. Rev.* **C75**, 054907 (2009).
 - [10] H. van Hee, M. Mannarelli, V. Greco, and R. Rapp, *Phys. Rev. Lett.* **100**, 192301 (2008).
 - [11] S. S. Cao, G. Y. Qiu, and S. A. Bass, *Phys. Rev.* **C88**, 044907 (2013).
 - [12] M. Nahrgang, J. Aichelin, P. B. Gossiaux, and K. Werner, *Phys. Rev.* **C93**, 044909 (2016).
 - [13] T. Song, H. Berrehrah, D. Cabrera, W. Cassing, and E. Bratkovskaya, *Phys. Rev.* **C93**, 034906 (2016).
 - [14] A. Beraudo, A. D. Pace, M. Monteno, M. Nardi, and F. Prino, *J. High Energy Phys.* **1802**, 043 (2018).
 - [15] J. F. Liao and E. Shuryak, *Phys. Rev. Lett.* **102**, 202302 (2009).
 - [16] J. C. Xu, J. F. Liao, and M. Gyulassy, *Chin. Phys. Lett.* **32**, 092501 (2015).
 - [17] S. K. Das, F. Scardina, S. Plumari, and V. Greco, *Phys. Lett.* **B747**, 260 (2015).
 - [18] J. C. Xu, J. F. Liao, and M. Gyulassy, *J. High Energy Phys.* **1602**, 169 (2016).
 - [19] J. Rafelski and B. Mddotuller, *Phys. Rev. Lett.* **48**, 1066 (1982).
 - [20] M. He, R. J. Fries, and R. Rapp, *Phys. Rev. Lett.* **110**, 112301 (2013).
 - [21] G. Aarts *et al*, *Eur. Phys. J.* **A54**, 93 (2017).
 - [22] S. Li, C. W. Wang, X. B. Yuan, and S. Q. Feng, *Phys. Rev.* **C98**, 014909 (2018).
 - [23] C. Shen, Z. Qiu, H. C. Song, J. Bernhard, S. A. Bass, and U. Heinz, *Comput. Phys. Commun.* **199**, 61 (2016).
 - [24] M. Cacciari, M. Greco, and P. Nason, *J. High Energy Phys.* **9805**, 007 (1998).
 - [25] M. Cacciari, S. Frixione, and P. Nason, *J. High Energy Phys.* **0103**, 006 (2001).
 - [26] M. Cacciari, S. Frixione, N. Houdeau, M. L. Mangano, P. Nason, and G. Ridolfi, *J. High Energy Phys.* **1210**, 137 (2012).
 - [27] K. J. Eskola, H. Paukkunen, and C. A. Salgado, *J. High Energy Phys.* **0904**, 065 (2009).
 - [28] I. Karpenko, P. Huovinen, and M. Bleicher, *Comput. Phys. Commun.* **185**, 3016 (2014).
 - [29] B. W. Zhang, E. K. Wang, and X. N. Wang, *Phys. Rev. Lett.* **93**, 072301 (2004).
 - [30] Guy D. Moore and D. Teaney, *Phys. Rev.* **C71**, 064904 (2005).
 - [31] V. Greco, *J. Phys. Conf. Ser.* **779**, 012022 (2017).
 - [32] D. Banerjee, S. Datta, R. Gavai, and P. Majumdar, *Phys. Rev.* **D85**, 014510 (2012).
 - [33] O. Kaczmarek, *Nucl. Phys.* **A931**, 633 (2014).
 - [34] H. T. Ding, A. Francis, O. Kaczmarek, F. Karsch, H. Satz, and W. Soeldner, *Phys. Rev.* **D86**, 014509 (2012).
 - [35] A. Francis, O. Kaczmarek, M. Laine, T. Neuhaus, and H. Ohno, *Phys. Rev.* **D92**, 116003 (2015).
 - [36] JET Collaboration, *Phys. Rev.* **C90**, 014909 (2014).
 - [37] T. Sjöstrand, S. Mrenna, and P. Z. Skands, *J. High Energy Phys.* **0605**, 026 (2006).
 - [38] C. Peterson, D. Schlatter, I. Schmitt, and P. M. Zerwas, *Phys. Rev.* **D27**, 105 (1983).
 - [39] P. D. B. Collins and T. P. Spiller, *J. Phys.* **G11**, 1289 (1985).
 - [40] E. Braaten, K. Cheung, and T. C. Yuan, *Phys. Rev.* **D48**, R5049 (1993).
 - [41] M. Cacciari, P. Nason, and R. Vogt, *Phys. Rev. Lett.* **95**, 122001 (2005).
 - [42] K. C. Han, R. J. Fries, and C. M. Ko, *Phys. Rev.* **C93**, 045207 (2016).
 - [43] R. Averbek, N. Bastid, Z. Conesa del Valle, P. Crochet, A. Dainese, and X. Zhang, [arXiv:1107.3243](#) (2011).
 - [44] ALICE Collaboration, [arXiv:1804.09083](#) (2018).
 - [45] ALICE Collaboration, *Eur. Phys. J.* **C77**, 550 (2017).
 - [46] ALICE Collaboration, *J. High Energy Phys.* **03**, 081 (2016).
 - [47] ALICE Collaboration, *Phys. Rev. Lett.* **120**, 102301 (2018).